Reprinted from MONTHLY WEATHER REVIEW, Vol. 119, No. 12, December 1991
American Meteorological Society

A Numerical Simulation of Amplification of Low-Frequency Planetary Waves and Blocking Formations by the Upscale Energy Cascade

H. L. TANAKA

Geophysical Institute, University of Alaska Fairbanks, Fairbanks, Alaska

(Manuscript received 30 July 1990, in final form 19 April 1991)

ABSTRACT

In this study, nonlinear numerical simulations of amplification of low-frequency planetary waves and concurrent blocking formations were performed. The simulations are conducted by a barotropic spectral model derived from three-dimensional spectral primitive equations with a basis of vertical structure functions and Hough harmonics. The model is truncated to include only barotropic Rossby components of the atmosphere with simple physics of biharmonic diffusion, topographic forcing, baroclinic instability, and zonal surface stress. These four physical processes are found to be sufficient to produce a realistic and persistent dipole blocking with a sharp transition from zonal to meridional flows on a sphere.

Analyzing energetics of blocking formations in the model, we showed an amplification of the meridional dipole mode was confirmed by means of the upscale energy cascade from synoptic disturbances under an environment of persistently amplified wavenumber 2. When the persistent wavenumber 2 exists, synoptic disturbances contribute to amplify the dipole mode of wavenumber 1. In contrast, when the persistent wavenumber 2 is absent, synoptic disturbances contribute to accelerate zonal flow with enhanced wave–mean flow interactions, and wavenumber 1 is not amplified. Therefore, we find that the persistent wavenumber 2 plays a catalytic role in drawing synoptic wave energy and feeding wavenumber 1. The topographic forcing in amplifying wavenumber 2 appears to be necessary for the blocking system in the model, although it is not the main energy source for the system.

1. Introduction

Amplification of low-frequency planetary waves in the troposphere is often coupled with a blocking formation. The importance of transient eddy forcing by synoptic disturbances to maintain low-frequency planetary waves has been a focus of interest in recent years. Many blocking episodes appear to be related to the transient eddy forcing. However, there are exceptions where enhanced transient eddy forcing failed to create blockings or blockings occurred without significant transient eddy forcing (see Wiin-Nielsen 1986; Shilling 1986). There is as yet no universally accepted theory of blockings, and the causal relationship of the amplification and blockings remains unclear.

Amplification of planetary waves in the troposphere implies an increase of the wave energy. If total atmospheric energy is partitioned in three energy boxes (zonal, planetary waves, and synoptic to short waves), there are only three paths by which planetary wave energy can increase (see Saltzman 1957): (i) downscale energy cascade from zonal to planetary wave energy; (ii) upscale energy cascade from synoptic and short wave to planetary wave energy; and (iii) energy supply from external forcing. Every theory describes a unique energy flow to excite the planetary waves. We can classify a number of theories using these three paths.

The first class—*downscale* energy cascade from zonal energy to planetary wave energy—includes instabilities of the zonal mean state (e.g., Chen and Shukla 1983; Shilling 1986). Atmospheric baroclinic instability transforms zonal available potential energy to planetary wave energy, whereas barotropic instability of a zonal jet transforms zonal kinetic energy to planetary wave energy. Recent energetics analyses by Sheng and Hayashi (1990) showed that the baroclinic conversion dominates the other energy supplies in the low-frequency variability. A vacillation phenomenon and an index cycle (Namias 1950) indicate downscale energy transformations from zonal energy to wave energy in the growing stage of planetary waves. The wave energy is then dissipated during the vacillation cycle. The underlying mechanism is the baroclinic instability of planetary waves. However, the growth rates in planetary waves are too small to explain the amplification by this mechanism alone.

The second class—*upscale* energy cascade from synoptic waves to planetary waves—is caused by the strong nonlinearity of wave–wave interactions. The synoptic waves are strongly excited by the baroclinic instability through the direct downscale cascade. The accumulated energy then yields upscale energy decascade toward planetary waves. It is known that the barotropic energy transformations are upscale, whereas the baroclinic

Corresponding author address: Dr. H. L. Tanaka, Institute of Geoscience, University of Tsukuba, Tsukuba, Ibanaki, 305 Japan.

energy transformations are downscale (see Tanaka and Kung 1988). Various observational analyses support this upscale energy cascade as the major energy source of low-frequency planetary waves (Hansen and Chen 1982; Holopainen and Fortelius 1987; Nakamura et al. 1987; Tanaka and Kung 1988; Kung et al. 1989). The upscale energy cascade, in general, is accompanied by energy transformations from high- to low-frequency variations. The reinforcement of the mean dipole-vorticity field by transient disturbances is demonstrated by Shutts (1983), Hains and Marshall (1987), Malanotte-Rizzoli and Malguzzi (1987), and Vautard and Legras (1988), among others. Further examination is desirable using spherical coordinates without a quasi-geostrophic assumption.

The third class—energy supply from *external forcing*—includes topographic forcing and thermal contrast of land–sea distributions. Linear resonant Rossby waves (Tung and Lindzen 1979) draw energy from topographic forcing of the same wavenumber when a free wave slows down and becomes in-phase with topographic forcing. Topographic instability (Charney and DeVore 1979) converts zonal energy into planetary waves via mountain torque, so it belongs partly to the first class. The surface topography plays a catalytic role in drawing zonal energy and feeding wave energy. The topographic instability tends to modify the basic state, so that the resonant phase speed of the system becomes closer to the forcing frequency (Plumb 1981).

According to Shilling's (1986) comprehensive analysis, blocking occurrence shows highest coherence with baroclinic instability of planetary waves, as in Sheng and Hayashi (1990). However, there are cases in which barotropic instability plays an important role, and cases in which the upscale energy cascade from synoptic disturbances dominates the other energy supplies. This suggests that the blocking system is excited by various energy sources from case to case, but reveals the same characteristic structures and behaviors. In the light of Shilling's puzzling results, Tanaka and Kung (1989) discussed a possibility that blockings can be understood as atmospheric eigenmodes excited by different energy sources from case to case. We intuitively understand the common persistent features as a low-frequency eigenmode. The characteristic structure may be understood such that the eigenvector has the dipole configuration. The eigenmode may be excited by various energy or vorticity supplies because it is a free mode. The positive and negative anomalies should have similar structures (see Dole 1986). We examined eigenmodes of low-frequency, unstable planetary waves in the zonally varying basic state, along the line of studies by Frederiksen (1982) and Frederiksen and Bell (1987), using spectral primitive equations on a sphere. Two different types of slow-moving Charney modes are found in planetary waves, showing different meridional structures. One of the Charney modes, M_1, is stationary at a preferred geographical location, indicating nearly barotropic structure. It resembles so-called Ω blockings in the atmosphere. The other Charney mode, M_2, indicates a dipole structure in the zonally varying basic state. The structures and behaviors of the dipole Charney mode markedly resemble dipole blockings in the atmosphere (see Fig. 1). We proposed that dipole Charney modes of wavenumber 1, which is modulated by the steady wavenumber 2, are responsible for large-scale dipole blocking, supported, for example, by the upscale energy cascade from synoptic disturbances. Yet, it is necessary to confirm the hypothesis using a fully nonlinear time-dependent model, because our previous results are based on a linear model under a restriction of small amplitudes.

The purpose of this study is to simulate the amplification of low-frequency planetary waves and concurrent blocking formations as realistically as possible, using a fully nonlinear spectral primitive equation model that is as simple as possible. The hypothesis of the blocking formation due to the upscale energy cascade from synoptic disturbances under the persistent wavenumber 2 is examined. The energy flows among different waves during blocking events are investigated in detail.

For that purpose, we construct a three-dimensional spectral primitive equation model with a basis of three-dimensional normal-mode functions (3D NMFs) for the motionless atmosphere (see Tanaka and Sun 1990). The model is then truncated to include only the barotropic component of the atmosphere. The contributions from the baroclinic components are parameterized as baroclinic–barotropic interactions. The model has simple physics of biharmonic diffusion, topographic forcing, baroclinic instability, and zonal surface stress. The upscale energy cascade from synoptic disturbances to planetary waves is achieved by the nonlinear wave–wave interactions. It will be shown that these combinations of physical processes are sufficient to produce a realistic and persistent dipole blocking with a sharp transition from zonal to meridional flows, although these may not be the necessary conditions.

The model description is given in detail in section 2. Section 3 describes the results of the simulation, including the time series, the gross energy budget, the synoptic features, and the energy flows during a blocking episode. The concluding summary of this study is given in section 4.

2. A description of the spectral primitive equation model

a. Prognostic equations

A system of primitive equations in a spherical coordinate of longitude λ, latitude θ, normalized pressure $\sigma = p/p_b$, and normalized time $\tau = 2\Omega t$ may be reduced

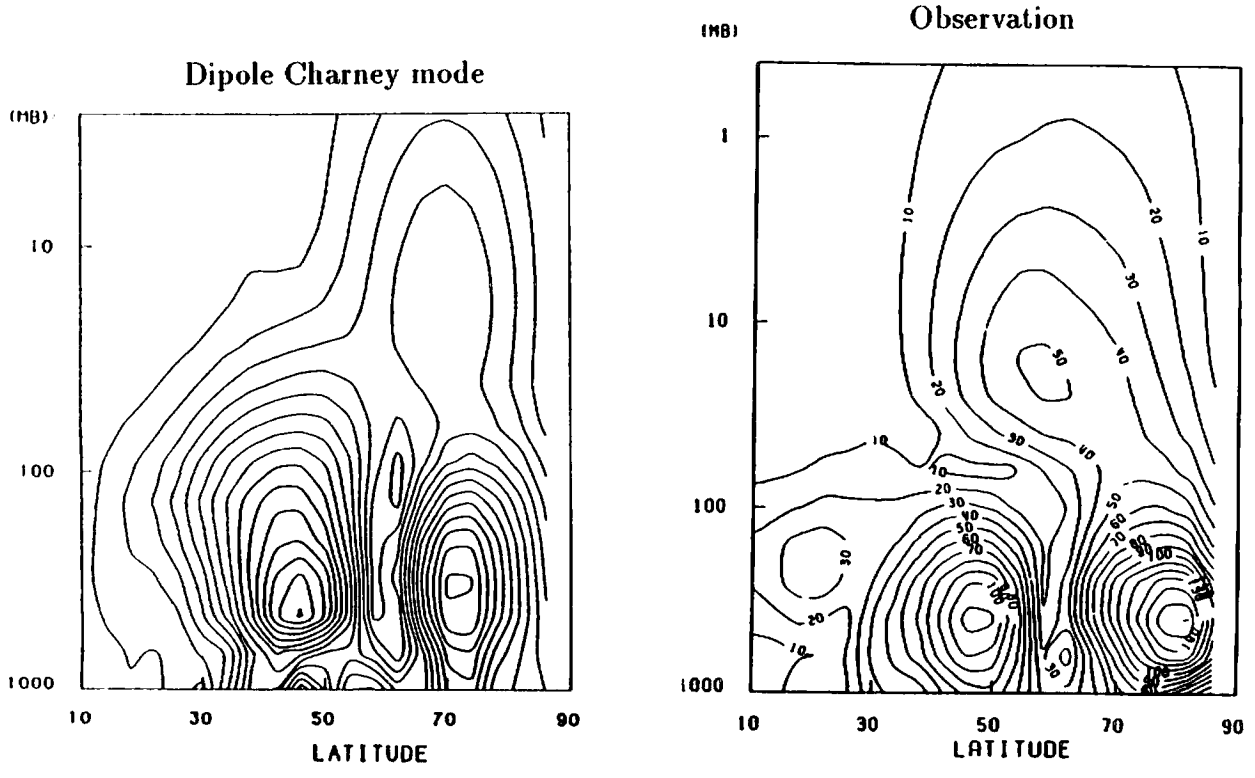

FIG. 1. Meridional–height section of the dipole Charney mode M_2 of $n = 1$ in the baroclinic atmosphere (see Tanaka and Kung 1989), compared with the observed dipole structure of $n = 1$ during the Pacific blocking in January 1979 (see Tanaka et al. 1989). Amplitudes of the geopotential height are multiplied by $\sigma^{1/2}$ to remove a density stratification effect.

to three prognostic equations of horizontal motions and thermodynamics. The three dependent variables are horizontal wind speeds, $\mathbf{V} = (u, v)$, and geopotential deviation ϕ from the global mean reference state. Using a matrix notation, these equations (refer to Tanaka and Sun 1990) may be written as

$$\mathbf{M}\frac{\partial}{\partial\tau}\mathbf{U} + \mathbf{L}\mathbf{U} = \mathbf{N} + \mathbf{F}, \tag{1}$$

where

$$\mathbf{U} = (u, v, \phi)^T, \tag{2}$$

$$\mathbf{M} = 2\Omega\ \mathrm{diag}\left(1, 1, -\frac{\partial}{\partial\sigma}\frac{\sigma^2}{R\gamma}\frac{\partial}{\partial\sigma}\right), \tag{3}$$

$$\mathbf{L} = \begin{bmatrix} 0 & -2\Omega\sin\theta & \dfrac{1}{a\cos\theta}\dfrac{\partial}{\partial\lambda} \\ 2\Omega\sin\theta & 0 & \dfrac{1}{a}\dfrac{\partial}{\partial\theta} \\ \dfrac{1}{a\cos\theta}\dfrac{\partial}{\partial\lambda} & \dfrac{1}{a\cos\theta}\dfrac{\partial(\ )\cos\theta}{\partial\theta} & 0 \end{bmatrix}, \tag{4}$$

$$\mathbf{N} = \begin{bmatrix} -\mathbf{V}\cdot\nabla u - \omega\dfrac{\partial u}{\partial\sigma} + \dfrac{\tan\theta}{a}uv \\ -\mathbf{V}\cdot\nabla v - \omega\dfrac{\partial v}{\partial\sigma} - \dfrac{\tan\theta}{a}uu \\ \dfrac{\partial}{\partial\sigma}\left(\dfrac{\sigma^2}{R\gamma}\mathbf{V}\cdot\nabla\dfrac{\partial\phi}{\partial\sigma}\right) \end{bmatrix}, \tag{5}$$

$$\mathbf{F} = \left(F_u, F_v, \frac{\partial}{\partial\sigma}\frac{\sigma Q}{c_p\gamma}\right)^T. \tag{6}$$

The symbols used in the equations are the earth's radius a, the angular speed of the earth's rotation Ω, the specific gas constant R, the specific heat at a constant pressure c_p, static stability parameter γ, the normalized vertical p velocity $\omega = d\sigma/dt$, the zonal F_u and meridional F_v components of frictional force, and the diabatic heating rate Q.

A 3D spectral representation of the primitive equations can be derived by taking an inner product of (1) and basis functions of the 3D normal-mode functions $\Pi_{nlm}(\lambda, \theta, \sigma)$,

$$\left\langle \mathbf{M}\frac{\partial}{\partial\tau}\mathbf{U} + \mathbf{L}\mathbf{U} - \mathbf{N} - \mathbf{F}, \mathbf{Y}_m^{-1}\Pi_{nlm}\right\rangle = 0. \tag{7}$$

where

$$\mathbf{\Pi}_{nlm}(\lambda, \theta, \sigma) = \mathbf{H}_{nlm}(\lambda, \theta)\mathbf{G}_m(\sigma), \quad (8)$$

$$\mathbf{Y}_m = 2\Omega \, \mathrm{diag}(\sqrt{gh_m}, \sqrt{gh_m}, 1), \quad (9)$$

and the inner product is defined as

$$\frac{1}{2\pi}\int_{-\pi/2}^{\pi/2}\int_0^{2\pi}\int_0^1 \mathbf{\Pi}^*_{nlm} \cdot \mathbf{\Pi}_{n'l'm'} \cos\theta d\sigma d\lambda d\theta = \langle \mathbf{\Pi}_{nlm}, \mathbf{\Pi}_{n'l'm'} \rangle = \delta_{nn'}\delta_{ll'}\delta_{mm'}. \quad (10)$$

Here $\mathbf{H}_{nlm}(\lambda, \theta)$ and $\mathbf{G}_m(\sigma)$ are Hough harmonics and vertical structure functions for zonal wavenumber n, meridional index l, and vertical index m, respectively. The scaling matrix $\mathbf{Y}_m$ is defined with the earth's gravity g and equivalent height h_m for every vertical index. Refer to Tanaka and Sun (1990) for the detail of the definitions and the derivation.

The resulting spectral primitive equations become a system of ordinary differential equations for Fourier expansion coefficients of variables

$$\frac{dw_i}{d\tau} + i\sigma_i w_i = -i\sum_{j=1}^{M}\sum_{k=1}^{M} r_{ijk}w_j w_k + f_i, \quad i = 1, 2, \cdots, M, \quad (11)$$

where w_i and f_i are the expansion coefficients of the dependent variables and diabatic processes, σ_i are Laplace's tidal frequencies, r_{ijk} are interaction coefficients, and M is the total number of the series expansion for the 3D atmospheric variables. Any choice of expansion basis functions with consistent boundary conditions will result in the representation of (11) after a proper diagonalization of the linear terms. The resulting expansion basis functions consist of vertical normal modes and Hough harmonics as in (8). The vertical normal modes consist of barotropic and baroclinic components, and the Hough harmonics comprise rotational and gravitational modes.

We demonstrated that observed basic features of blockings can be represented by their barotropic components. Based on this observed fact, we collect only the barotropic components of the expansion coefficients with the index $m = 0$ in (7):

$$\left\langle \mathbf{M}\frac{\partial}{\partial\tau}\mathbf{U} + \mathbf{LU} - \mathbf{N} - \mathbf{F}, \mathbf{Y}_0^{-1}\mathbf{\Pi}_{nl0} \right\rangle = 0. \quad (12)$$

The corresponding spectral equations are

$$\frac{dw_i}{d\tau} + i\sigma_i w_i = \langle \mathbf{N}, \mathbf{Y}_0^{-1}\mathbf{\Pi}_{nl0} \rangle + f_i, \quad i = 1, 2, \cdots, N, \quad (13)$$

where N is the total number in the series expansion for the barotropic model. The right-hand side of (13) is parameterized in this study as

$$\langle \mathbf{N}, \mathbf{Y}_0^{-1}\mathbf{\Pi}_i \rangle = -i\sum_{j=1}^{N}\sum_{k=1}^{N} r_{ijk}w_j w_k + (\mathrm{BI})_i, \quad i = 1, 2, \cdots, N, \quad (14)$$

and

$$f_i = (\mathrm{DF})_i + (\mathrm{TF})_i + (\mathrm{ZS})_i, \quad (15)$$

where $(\mathrm{BI})_i$, $(\mathrm{DF})_i$, $(\mathrm{TF})_i$, $(\mathrm{ZS})_i$ are, respectively, the formal source–sink terms derived from baroclinic instability, diffusion, topographic forcing, and zonal surface stress to be described later. In (14) the quadratic products of w_i for the barotropic component are explicitly evaluated. Therefore, the nonlinear wave–wave and zonal-wave interactions are treated accurately as a barotropic model. The rest of the nonlinear terms describes barotropic–baroclinic interactions. We consider only baroclinic instability among various possible processes that cause the barotropic–baroclinic interactions. Given these formal source–sink terms, the nonlinear equation (13) becomes a closed system of the prognostic equation.

It is important to notice that a diabatic heating rate Q for the barotropic component vanishes under a minor assumption of neglecting $dG_0/d\sigma$, since Q may be assumed to be zero in the subterranean regions:

$$\int_0^1 \frac{\partial}{\partial\sigma}\left(\frac{\sigma Q}{c_p\gamma}\right)G_0 d\sigma \approx \int_0^1 \frac{\partial}{\partial\sigma}\left(\frac{\sigma Q}{c_p\gamma}\right)d\sigma = 0, \quad (16)$$

where G_0 is a vertical structure function of the barotropic component. Every heat-related energy source in the atmosphere goes to the baroclinic components, and the energy is then transformed into the barotropic component through the baroclinic–barotropic interactions. The complicated heating fields produced by numerous physical processes are reduced to the single concept of the baroclinic–barotropic interaction.

Parameterizing a physical process based on a possible energy gap in the spectral domain is desirable. The energy gap should separate the resolvable large-scale process from the unresolvable small-scale process to be parameterized. Although there is no such ideal energy gap in the horizontal energy spectrum, a clear energy gap in the vertical energy spectrum can be observed between the baroclinic and barotropic component (e.g., Tanaka 1985; Silva Dias and Bonatti 1986). Therefore, the construction of a barotropic primitive-equation model with energy sources from the baroclinic component can be a viable method for understanding the general circulation and the low-frequency variability of the atmosphere.

b. Diffusion

For large-scale atmospheric motions, an eddy momentum transfer by the Reynolds stress dominates the

viscous stress. The Reynolds stress is initially and in reality a nonlinear contribution in (11) for unresolvable (high-frequency) motions. In this study, we attempted to parameterize the scale dependency of diffusion using the 3D scale index σ_i based on the wave dispersion relating wave scale and wave frequency. The biharmonic-type diffusion for the Rossby (rotational) wave dispersion (for wavenumber $n \neq 0$) is approximated by

$$(\mathrm{DF})_i = -K\left(\frac{n}{\sigma_i}\right)^2 w_i, \tag{17}$$

where K is a diffusion coefficient and $K(2\Omega a^4) = 2.0 \times 10^{16}\ \mathrm{m^4\ s^{-1}}$. Haurwitz waves on a sphere have phase speeds represented by the total wavenumber of the spherical surface harmonics $\hat{l}$ (see Swarztrauber and Kasahara 1985):

$$c = \frac{-1}{\hat{l}(\hat{l}+1)} \approx \frac{\sigma_i}{n}. \tag{18}$$

The rotational Hough modes are known to converge to Haurwitz waves in the limit, as an equivalent height h_m tends to infinity. For the barotropic component, $m = 0$, a realistic temperature profile gives $h_0 = 9623.9$ m. Since the diffusion is often approximated with $\hat{l}(\hat{l}+1)$, the present form of diffusion in (17) approaches the biharmonic-type diffusion for higher-order rotational modes. For the zonal component, the meridional index l_R is substituted for $\hat{l}$. Note that the same form of diffusion is automatically imposed on geopotential field as well as wind field.

Similar approximation leads to a diffusion for nondispersive gravity modes as

$$(\mathrm{DF})_i = -K\frac{(2\Omega a\sigma_i)^4}{(gh_0)^2} w_i. \tag{19}$$

because the phase speed of gravity modes (e.g., Andrews et al. 1987) is given by

$$c^2 = \frac{gh_0}{(2\Omega a)^2} \approx \frac{\sigma_i^2}{\hat{l}(\hat{l}+1)}. \tag{20}$$

It is found that the diffusion parameterization in the frequency domain is distinctly different for Rossby modes and gravity modes. The diffusion of Rossby modes depends solely on the inverse of the phase speed, whereas that of gravity modes depends solely on the frequency.

c. *Topographic forcing*

A kinematic uplift of an air column by the surface topography H is originated by a horizontal component of the normal stress of the topography. It has been parameterized by a forced upward motion w, which is induced by the barotropic flow V_0. Because our model atmosphere is compressible and w is zero in the subterranean regions, we must assume the vertical profile of w. The topographic effect for the barotropic component w_0 is parameterized by

$$w_0 = \int_0^1 \frac{w}{h_0}\, d\sigma = k\mathbf{V}_0 \cdot \nabla \frac{H}{h_0}, \tag{21}$$

where k is a constant depending on the profile of w. Charney and Eliassen's (1949) original work uses $k = 0.4$. The spectral representation of (21) becomes $(\mathrm{TF})_i$ in (15):

$$(\mathrm{TF})_i = \langle (0, 0, w_0)^T, \mathbf{Y}_0^{-1}\mathbf{\Pi}_{n0} \rangle. \tag{22}$$

There is some arbitrariness in the choice of $k\mathbf{V}_0$; e.g., Jacqmin and Lindzen (1985) use the 1000-mb wind, Chen and Trenberth (1988) use the 850-mb wind, and Valdes and Hoskins (1989) use the true surface wind. There is no wind at the true surface in our model. Therefore, k is combined with H, and an idealized topography of wavenumber 2 is used

$$kH(\lambda, \theta) = -A \sin^2(\pi\mu^2)\cos(2\lambda), \tag{23}$$

where $A = 400$ m and $\mu = \sin\theta$. The peak is located at 45°N, 90°E and 45°N, 90°W.

d. *Baroclinic instability*

Zonal available potential energy produced by differential heating is transformed to eddy barotropic energy. The energy flow is characterized by a sequence of energy transformations from zonal baroclinic to eddy baroclinic and to eddy barotropic components. The eddy barotropic energy is further transformed to zonal barotropic energy (see the Appendix; Wiin-Nielsen 1962; Smagorinsky 1963). The maximum supply to the barotropic energy occurs at the synoptic waves (see Tanaka and Kung 1988). Baroclinic instability in midlatitudes is responsible for this energy transformation. Since the most important part of the baroclinic–barotropic interaction is related to the baroclinic instability, the parameterization of this process is essential for the construction of a barotropic model. This process has been ignored in many shallow-water-equation models on the sphere.

First consider trajectories of $w_i(\tau)$ in (11) for baroclinic atmosphere. When the amplitude of $w_i(\tau)$ for eddies is small compared with that of the zonal component, the direction to which $w_i(\tau)$ grows can be predicted; this direction is the unstable subplace ξ_i due to the atmospheric baroclinic instability, predicted by a linear theory. Given a zonal field, the structure ξ_i and the growth rate ν are known (see Tanaka and Kung 1989). When $w_i(\tau)$ grows along the unstable subspace, both the baroclinic and barotropic components of $w_i(\tau)$ will grow exponentially, maintaining the consistent structure. The energy increases in the barotropic and baroclinic components are synchronized with each other. It is in this process that the zonal baroclinic en-

ergy is transformed to the eddy barotropic energy. The growth of the barotropic components can be predicted by the linear process with known ξ_i. Based on this concept, parameterization of the atmospheric baroclinic instability for (13) has been attempted by calculating the orthogonal projection of the barotropic expansion coefficients $w_i(\tau)$ onto the barotropic component of the prescribed ξ_i:

$$w_i(\tau) = a(\tau)\xi_i + \epsilon_i(\tau), \tag{24}$$

where ξ_i has a unit norm, $\epsilon_i(\tau)$ is the orthogonal complement of the projection, and $a(\tau)$ is calculated from $w_i(\tau)$ every time step:

$$a(\tau) = \sum_i w_i(\tau)\xi_i^*. \tag{25}$$

By differentiating (24) with respect to τ, the predicted growth due to the instability is obtained:

$$(\mathrm{BI})_i = \frac{da(\tau)}{d\tau}\xi_i = -i\nu a(\tau)\xi_i, \tag{26}$$

where ν is the complex eigenvalue of the stability problem associated with ξ_i. In the Appendix, the baroclinic and barotropic wave growth and the parameterized barotropic growth are compared using a nonlinear baroclinic model. It is evident in the Appendix that the parameterization is accurate for a small amplitude of w_i, as the linear theory predicts. Tanaka and Sun (1990) suggest that this process operates even for finite-amplitude planetary waves. The monthly mean zonal basic state for January 1979 is used to obtain the eigenpair of ν and ξ_i. The growth rates and phase speeds used in this study are listed in Table 1. This parameterization based on a prescribed zonal baroclinic energy field causes a major energy source of the barotropic model atmosphere. As the synoptic waves grow due to the baroclinic energy source, the increased wave energy starts to cascade to other waves and zonal flow by the wave–wave and zonal-wave interactions. These two competing effects of the energy source and the nonlinear scattering ultimately equilibrate to a wave saturation. It will be shown that the resulting energy spectra are consistent with observed energy spectra (see Fig. 5).

e. Zonal surface stress

As the waves grow, the nonlinear zonal-wave interaction begins to accelerate the zonal flow. A northward shift of the subtropical jet occurs due to the northward eddy momentum transport induced by the waves. For the barotropic flow, the important physics that must be considered to balance the northward shift of the jet are the surface stress and mountain torque. The westerly deceleration in the midlatitudes and the easterly deceleration in the low latitudes should balance with the northward eddy momentum flux. We adopt the following parameterization of the zonal surface stress:

TABLE 1. Mode name, growth rates (day^{-1}), and phase speeds (deg day^{-1}) of the baroclinically unstable modes for wavenumbers n = 1–6; M_2 is the dipole Charney mode and M_C the shallow Charney mode.

n	1	2	3	4	5	6
Mode	M_2	M_2	M_2	M_2	M_C	M_C
Growth rate	0.06	0.11	0.15	0.18	0.25	0.35
Phase speed	8.9	9.1	9.0	8.6	8.1	8.4

$$(\mathrm{ZS})_i = -\alpha(w_i - \bar{w}_i) \quad \text{for} \quad n = 0, \tag{27}$$

where $\bar{w}_i$ is the monthly mean for January 1979, and $\alpha(2\Omega) = 2.32 \times 10^{-6}\ \mathrm{s}^{-1}$, which corresponds to the relaxation time of 5 days. Similar relaxation is seen for barotropic models by Charney and DeVore (1979), Juckes (1989), and Salby et al. (1990).

f. Numerical scheme and initial condition

The system of nonlinear equations (13) is truncated to include only the barotropic Rossby modes for m = 0, n = 0–6, and l_R = 0–19. We noted that the low-frequency variability has a planetary-wave scale with an equivalent barotropic structure. The truncation is imposed in the frequency domain as well as in the wavenumber domain by excluding high-frequency gravity modes. We made the simplest model that still retains realistic blockings in the model atmosphere. The initial condition is a northern zonal field of January 1979, which is symmetric about the equator. Small amplitude random disturbances are superimposed on the initial zonal field. The time integration is based on a combination of leapfrog and periodic use of an Euler-backward scheme with a time step of 1 h. By virtue of the closure with the low-frequency subspace, our model requires no implicit scheme and no artificial smoothing.

3. Results of the simulation

a. Time series

We examine first the basic features of the simulation results because the numerical model in terms of the 3D NMF expansion is relatively new. A similar model experiment was conducted by Kasahara (1977), using shallow-water equations. By his demonstration, the utility of a Hough mode expansion for a nonlinear model has been established as an alternative approach to the standard spectral methods. In contrast to Kasahara's model, our model is derived from 3D primitive equations, and our model includes energy sources and sinks in a highly parameterized form. A nonlinear simulation of a Haurwitz wave was conducted (Phillips 1959) by eliminating all physics. The results agree well with previous numerical experiments (e.g., Kasahara 1977; Holloway et al. 1973).

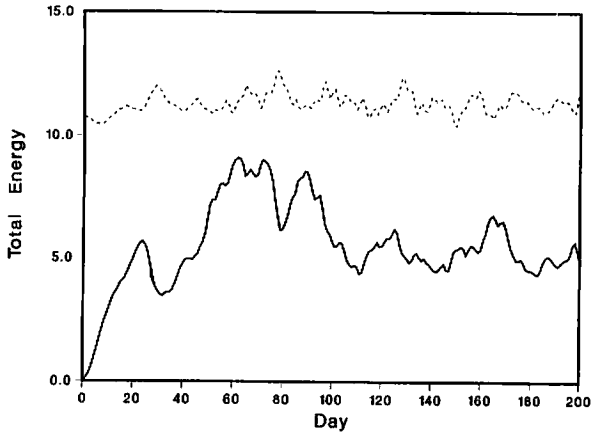

FIG. 2. Time series of zonal energy (dashed line) and eddy energy (solid line) of the model atmosphere for days 0–200. Units are 10^5 J m^{-2}.

The results of the numerical integration are shown first for the time series of zonal (dashed line) and eddy (solid line) energies in Fig. 2. The eddy energy (n = 1–6) increases during the first 20 days. This period is regarded as an initial adjustment against the model's external forcing. After a slight decrease, the energy increases again during days 40–60. The second energy peak occurs around days 60–70. The peak energy level is about 8×10^5 J m^{-2}. Then the energy level fluctuates around 6×10^5 J m^{-2} for the rest of the integration period. Zonal energy fluctuates around the initial value of 11×10^5 J m^{-2}.

In Fig. 3, the eddy energy is split into n = 1 (dashed line), n = 2 (solid line), and the sum of n = 3–6 (dotted line). It is clear that the initial growth of eddy energy is caused by topographic forcing of n = 2. The energy level of n = 2 fluctuates around 2×10^5 J m^{-2} after day 30. There is a steady increase of n = 3–6 until day 40. The energy level is high (exceeding 4×10^5 J m^{-2}) for days 50–100, but it is low (about 2×10^5 J m^{-2}) after day 100. The energy of n = 1 increases after day 40, and the energy peak (about 4×10^5 J m^{-2}) occurs around day 60. During this peak of n = 1, a pronounced blocking appears in the model atmosphere.

Figure 4 illustrates latitude–time cross sections of zonal wind speed and geopotential height amplitudes for n = 1 and 2. The subtropical barotropic jet stays near 40°N, indicating maximum speed of 18 m s^{-1}. Large variations are seen at the northern flank of the jet, showing occasional intrusion of westerly momentum into high latitudes. A persistent easterly develops in the tropical zone and another intermittent easterly develops in the Arctic. Wavenumber 1 indicates large amplitude of geopotential height exceeding 200 m for days 45–75 and for days 90–105. The latitude of the maximum amplitude is near 75°N for the first peak and 65°N for the second peak. A notable event of a meridional dipole structure of amplitude takes place around day 60. The peak amplitudes are located at 75° and 55°N. A dipole blocking occurs during this period as the meridional dipole of n = 1 develops. Wavenumber 2 shows the initial amplification by topography near 65°N. The amplitude maximum exceeds 200 m. In the subsequent time integration, large amplitudes exceeding 200 m appear episodically.

b. *Gross energy budget*

According to Tanaka (1985), the total energy E_i for each basis function is defined in a dimensional form by

$$E_i = \frac{1}{2} p_b h_0 |w_i|^2. \tag{28}$$

By differentiating with respect to time and substituting (13)–(15), the energy balance equation,

$$\frac{dE_i}{dt} = \mathrm{NL}_i + \mathrm{DF}_i + \mathrm{TF}_i + \mathrm{BI}_i + \mathrm{ZS}_i, \tag{29}$$

is obtained, where

$$\begin{aligned}
\mathrm{NL}_i &= p_b h_0 \Omega [w_i^* (\mathrm{NL})_i + w_i (\mathrm{NL})_i^*], \\
\mathrm{DF}_i &= p_b h_0 \Omega [w_i^* (\mathrm{DF})_i + w_i (\mathrm{DF})_i^*], \\
\mathrm{TF}_i &= p_b h_0 \Omega [w_i^* (\mathrm{TF})_i + w_i (\mathrm{TF})_i^*], \\
\mathrm{BI}_i &= p_b h_0 \Omega [w_i^* (\mathrm{BI})_i + w_i (\mathrm{BI})_i^*], \\
\mathrm{ZS}_i &= p_b h_0 \Omega [w_i^* (\mathrm{ZS})_i + w_i (\mathrm{ZS})_i^*].
\end{aligned} \tag{30}$$

The term $(\mathrm{NL})_i$ is the nonlinear term in (14). Similar symbols to those in (15) are used, but without the parenthesis for real-valued energy variables of dynamical and physical processes. Note that the linear term in

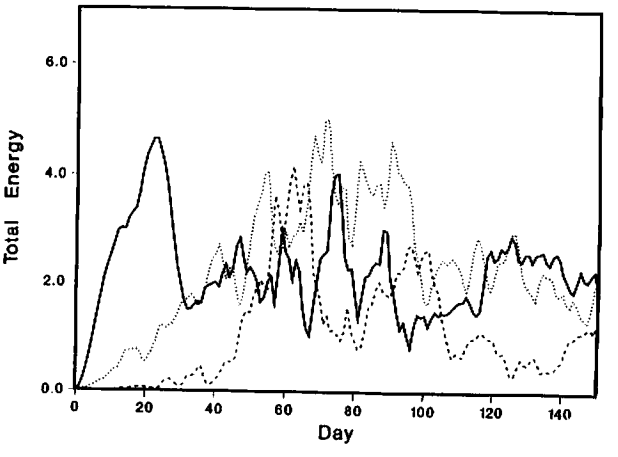

FIG. 3. Time series of total energy of zonal wavenumber n = 1 (dashed line), n = 2 (solid line), and the sum of n = 3–6 (dotted line). Units are 10^5 J m^{-2}.

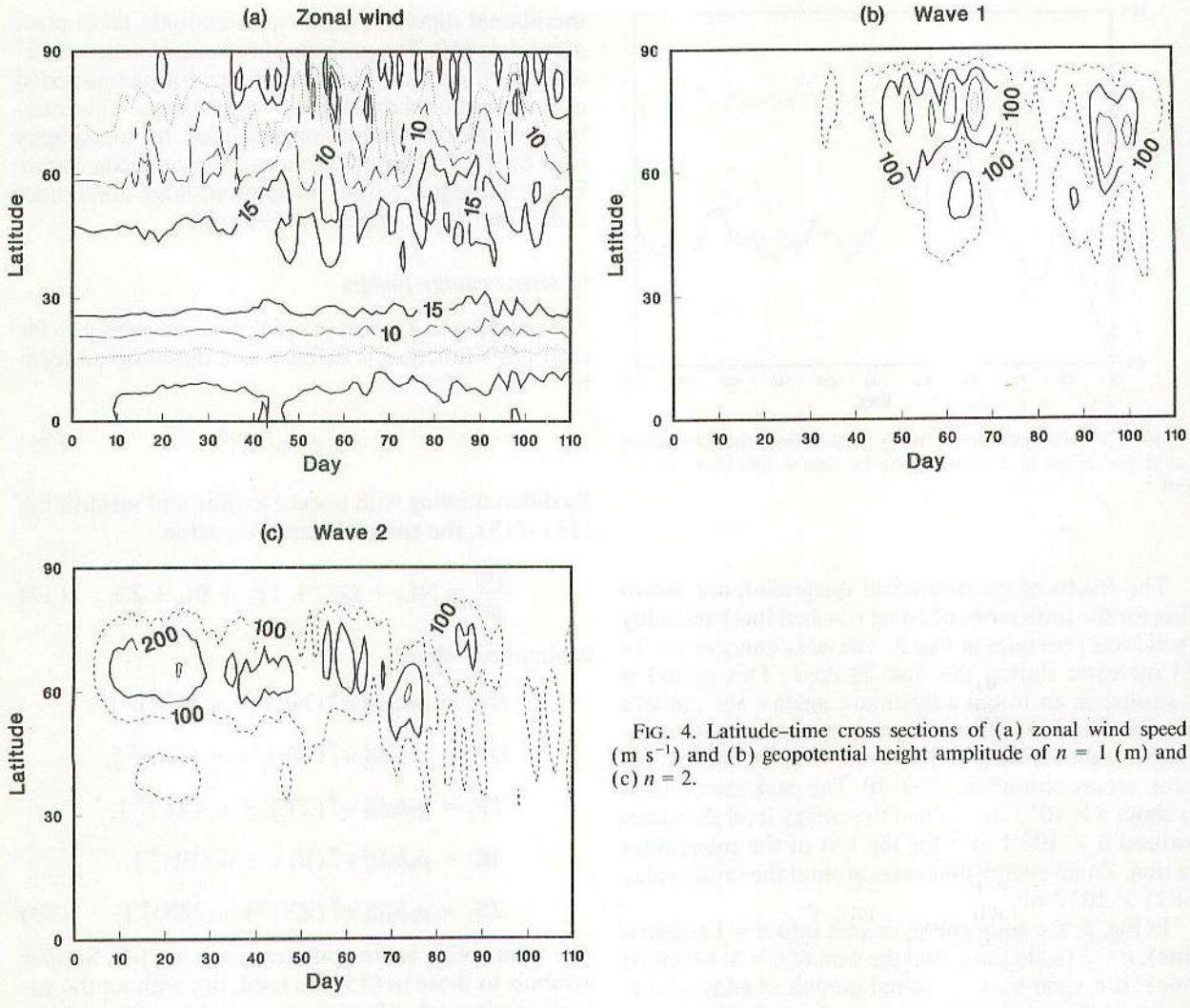

FIG. 4. Latitude–time cross sections of (a) zonal wind speed (m s^{-1}) and (b) geopotential height amplitude of $n = 1$ (m) and (c) $n = 2$.

the left-hand side of (13) does not contribute to the energy balance equation.

The results of time mean (days 30–200) energy spectra for $n = 1$–6 are illustrated in Fig. 5 as functions of the 3D scale index $|\sigma_i|$. There is an energy peak of $n = 2$ at $|\sigma_i| = 0.04$. The peak of $n = 1$ is seen at the lower frequency ($|\sigma_i| = 0.02$) and the peak of $n = 3$ at the higher frequency ($|\sigma_i| = 0.08$) relative to that of $n = 2$. Wavenumber 6 indicates the peak at $|\sigma_i| = 0.05$. These peaks are qualitatively similar to observed spectral peaks (Tanaka and Sun 1990).

The energy variables are summed for all meridional indices and averaged for days 30–200. The results of the energy and energy transformations are summarized in Table 2 for $n = 0$–6. The eddy energy is largest at $n = 2$ and second largest at $n = 1$. The higher wavenumbers contain less energy. The mean energy levels of the results are comparable to those of the real atmosphere. There are two major energy sources, the topographic energy source at $n = 2$ and the baroclinic energy source at $n = 6$. The energy is then redistributed by the nonlinear interactions toward $n = 0$. As in observation, $n = 1$ receives energy through the nonlinear interactions. There is a main energy sink at $n = 0$ from the zonal surface stress. Diffusion is rather evenly distributed over the waves. The important role of the nonlinear triad interactions is evident in energy transfer from the source at $n = 2$ and 6 to the sink at $n = 0$. The transfer is characterized as the upscale cascade from small-scale motions to large-scale motions. Further improvement of the model may be possible by adding more physics. However, the fundamental energy flow seems to have been expressed by this simplest combination of the physical processes. Our simple model already has the capability of producing realistic and persistent blockings. Therefore, it is meaningful to analyze the low-frequency variability of planetary waves in the model in conjunction with the blocking episode.

c. *Synoptic features of a blocking episode*

Although there are a number of variations, blocking may be defined as a high pressure system that persis-

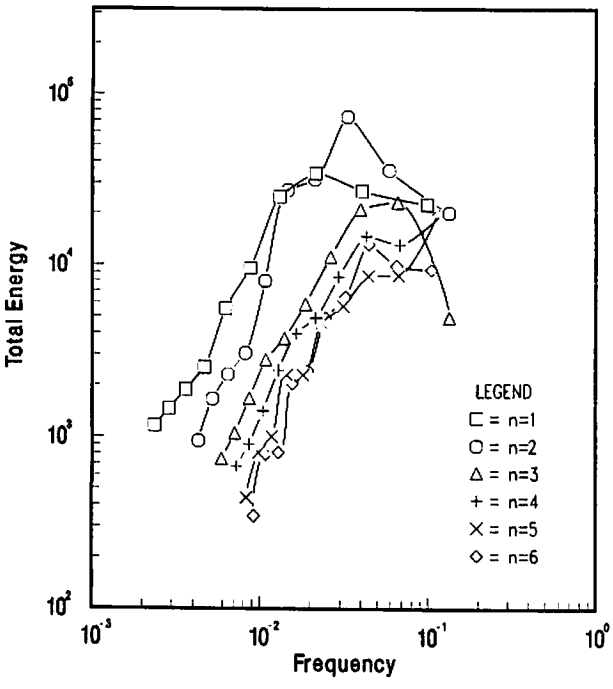

FIG. 5. Time-mean (days 30–200) energy spectra (J m^{-2}) as functions of the dimensionless eigenfrequency $|\sigma_i|$ in (1) for wavenumbers n = 1–6. The frequency in the abscissa represents the modal 3D scale due to the intrinsic dispersion relation of normal modes.

tently blocks the subtropical jet. This definition is based on its characteristic persistence (the low-frequency nature) and its characteristic structure of a high pressure system (dipole or Ω structure). A more quantitative definition is given as a large-scale persistent anomaly (e.g., Dole 1986). These definitions do not include any restriction for the intrinsic cause.

Figure 6 illustrates daily barotropic geopotential fields during days 54–69. Illustrated is the period when wavenumber 1 amplifies persistently, indicating a meridional dipole structure (see Fig. 4). The barotropic geopotential field roughly corresponds to the 500-mb height field. The coastal line is drawn for reference in the model results. During days 54–56, the blocking system developed near 45°W, indicating a progression. A stretched polar vortex began to split into two vortices along 90°E and 90°W. Clearly wavenumber 2 amplified with its troughs along 90°E and 90°W. A dipole blocking emerged with its high pressure center at 60°N, 45°W. The location corresponds to 45° downstream of the major trough along 90°W. During days 57–60, the dipole blocking entered its first mature stage. The geopotential height near 60°N is 300 m higher than surrounding area. The polar vortex developed along 90°W, then it migrated to 90°E through the North Pole. During days 61–62, the high pressure cell decayed and deformed as a cutoff low progressed over the East Coast. During days 63–65, the blocking high entered its second mature stage. The migrating cutoff low was blocked by the blocking high. The southern low, associated with the blocking, began to progress. During days 66–67, this southern low ultimately evanesced, and the blocking indicated an intermission. During days 68–69, the ridge developed again and the blocking showed the third mature stage; this time it was the Ω blocking. A strong cutoff low progressed upstream of the Ω blocking by which the blocking eventually disappeared.

The results described above reasonably resemble observed blocking evolution. A sharp transition from zonal to meridional flow is clear at the upstream of the blocking system. The persistency of the system is more than two weeks. Our simple nonlinear barotropic model seems to capture the essential mechanism of the blocking system. We can conclude, at least, that the blocking can be simulated using a barotropic model with four physical processes of diffusion, topographic forcing, baroclinic instability, and zonal surface stress. It is interesting to observe not only the blocking but the developing synoptic waves. For example, a weak trough along 150°E on day 58 progressed and was developed by the parameterized baroclinic instability.

d. Energy budget during the blocking episode

The amplification of the meridional dipole structure of n = 1 is found to be important for the development of the large-scale dipole blocking. The blocking structure also requires the amplification of n = 2. We demonstrated that a model run without topography fails to simulate the large-scale blocking because the planetary waves were not amplified. Amplification of these low-frequency planetary waves is necessary for blocking formations. To analyze the cause of the amplification of n = 1 and 2, an energy budget analysis is conducted for low-frequency variations during the blocking period.

If the long-term means of the energy variables in Table 2 are subtracted from the energy equation (29), we obtain an energy balance equation for transient variations indicated by primes:

TABLE 2. Averaged energy variables for wavenumbers n = 0–6 during days 30–200. The symbols designate total energy E_n, nonlinear interaction NL_n, diffusion DF_n, topographic forcing TF_n, baroclinic instability BI_n, and zonal surface stress ZS_n. The units are 10^3 J m^{-2} for energy and 10^{-3} W m^{-2} for energy transformations.

n	E_n	NL_n	DF_n	TF_n	BI_n	ZS_n
0	1136	258	−11	−44	0	−203
1	131	25	−28	0	11	0
2	204	−185	−54	207	32	0
3	76	4	−35	3	31	0
4	72	−9	−39	9	39	0
5	56	−15	−38	−2	58	0
6	50	−83	−48	−2	138	0

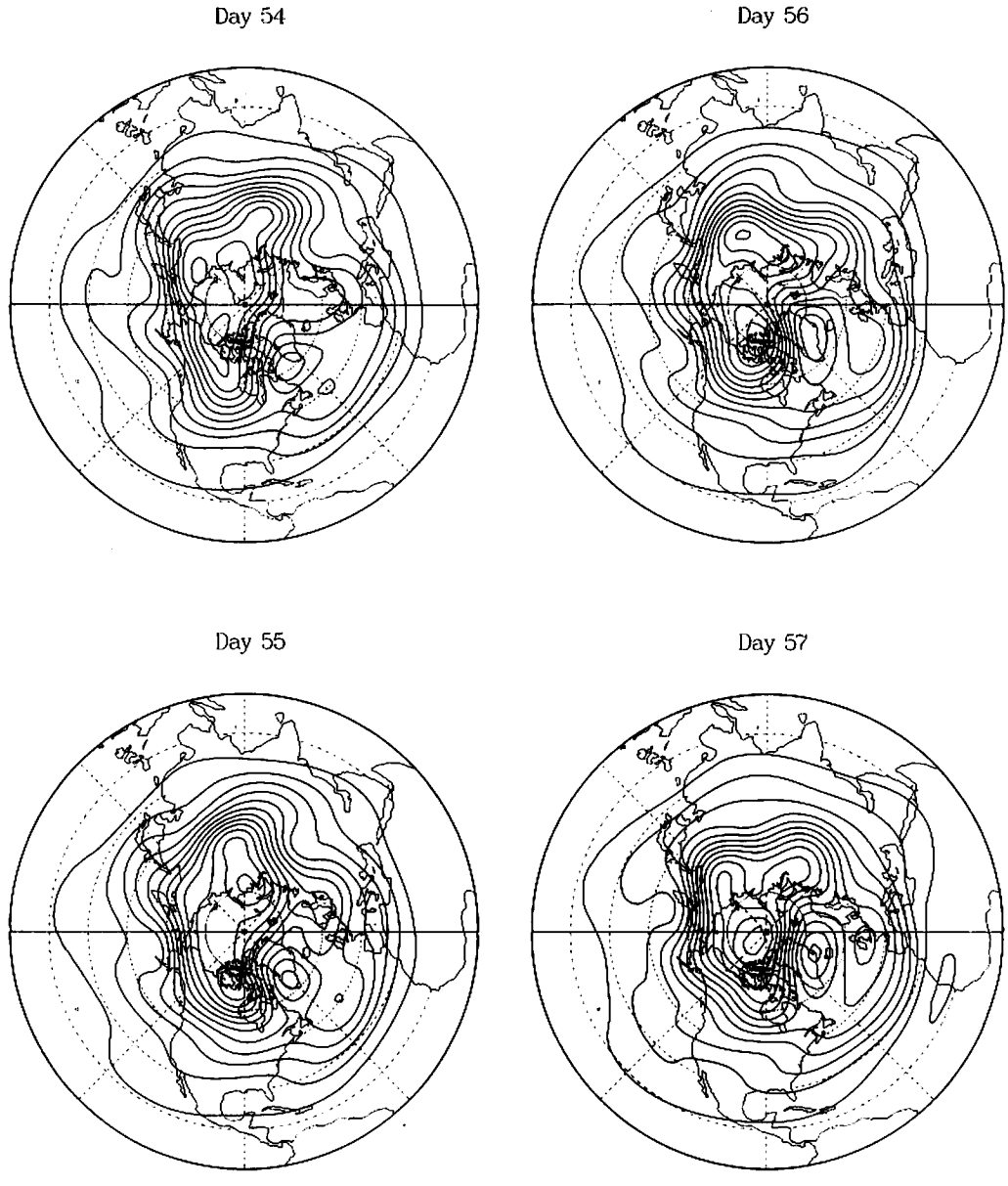

FIG. 6. Daily geopotential fields during days 54–69 when a blocking occurred in the model atmosphere. The contour interval is 100 m.

$$\frac{dE_i}{dt} = \mathrm{NL}_i' + \mathrm{DF}_i' + \mathrm{TF}_i' + \mathrm{BI}_i' + \mathrm{ZS}_i'. \quad (31)$$

An integration with respect to time yields

$$E_i(t) - E_i(t_0) = \int_{t_0}^{t} \mathrm{NL}_i'\,dt + \int_{t_0}^{t} \mathrm{DF}_i'\,dt + \int_{t_0}^{t} \mathrm{TF}_i'\,dt + \int_{t_0}^{t} \mathrm{BI}_i'\,dt + \int_{t_0}^{t} \mathrm{ZS}_i'\,dt. \quad (32)$$

The equation shows that the transient energy increase or decrease, $E_i(t) - E_i(t_0)$, from a certain base time t_0 is caused by the integrals in the right-hand side of (32). The integrals represent energy evolution expected from the transiency of individual dynamical and physical processes. The sum of the energy evolution for the right-hand side of (32) must agree with $E_i(t) - E_i(t_0)$. Since the integral operator emphasizes a low-frequency transiency, we can analyze the low-frequency variability of energy field from the comparison of computed energy evolution.

The results of the energy budget of low-frequency variations during the blocking period are illustrated in Fig. 7. The base time was chosen at day 40. The time evolution of solid lines are the same as in Fig. 3, except for a shift by $E_i(t_0)$. The results show that the amplification of $n = 1$ is caused by nonlinear wave–wave

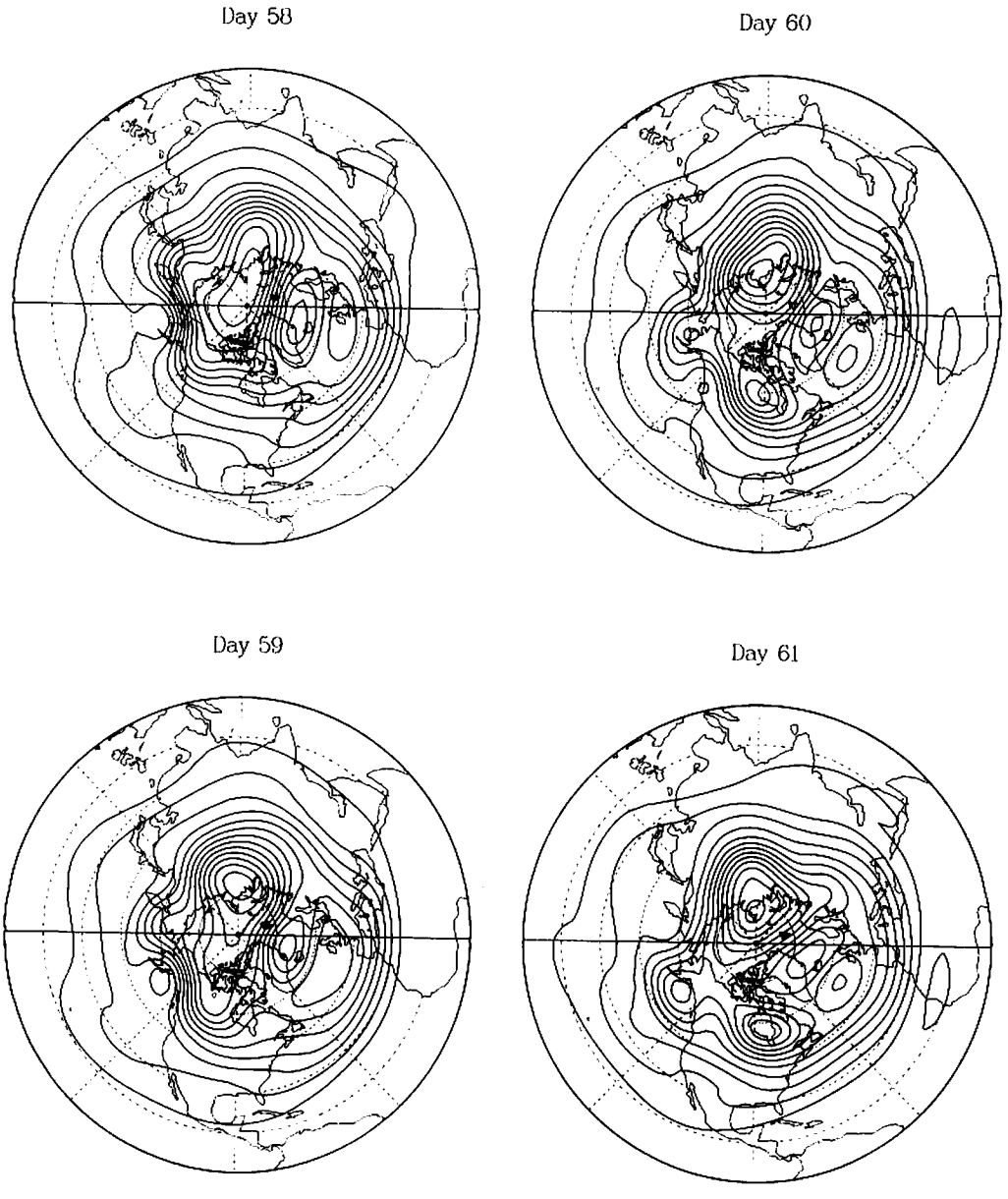

FIG. 6. (*Continued*)

interactions NL_i. The low-frequency variation of $n = 1$ is almost completely explained by NL_i, and other physical processes show secondary importance. The energy variation for $n = 2$ is caused by two competing processes of topographic forcing TF_i and the nonlinear scattering NL_i. During the amplification of $n = 1$, wavenumber 2 draws energy from topographic forcing and feeds the energy for other waves through the nonlinear interactions. It is enticing to support the topographic origin for the amplification of wavenumber 1. Contrasted with the smooth variation of TF_i, NL_i contains both the high- and low-frequency variability. The low-frequency part cancels out and only the high-frequency part appears in energy variation. The zonal motion receives the largest part of the nonlinear interactions (see Table 2). Yet, the transiency in $n = 0$ is considerably small relative to the large energy level and steady energy transformations. This result is consistent with observations.

The important problem is to show from where the energy of $n = 1$ is transformed. Every triad wave–wave interaction must satisfy a wavenumber rule $n = n' + n''$. For $n = 1$ the triad interactions (n, n', n'') can be classified in three types: downscale self-interactions with $n = 0$, that is, $(1, 0, 1)$; upscale self-interactions with $n = 2$, that is, $(1, -1, 2)$; and the rest of upscale triad interactions of $(1, -2, 3)$, $(1, -3, 4)$, $(1, -4, 5)$, and $(1, -5, 6)$. Any upscale interaction toward smaller

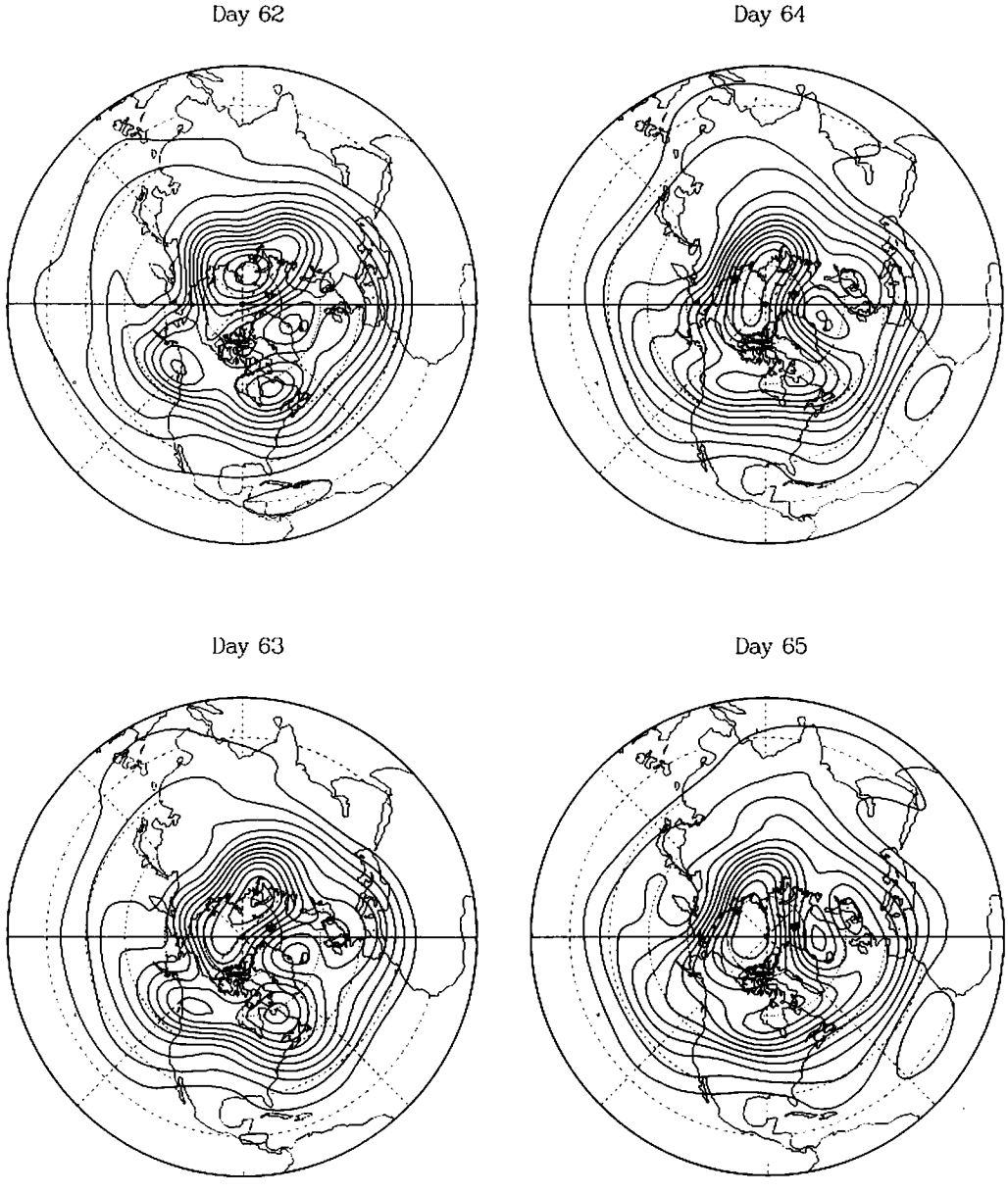

FIG. 6. (*Continued*)

wavenumber involves a triad combination with a negative wavenumber. The negative wavenumber appears as a complex conjugate term in Eq. (11), and its mathematical role in the system is quite different from that of a positive wavenumber (see Tanaka and Kung 1989). The nonlinear wave–wave interactions of $n = 1$ in Fig. 7 are further divided in contributions from these three types of interactions (see Fig. 8). The chain–dot line (1, 0, 1) describes zonal-wave interactions of ordinary barotropic conversion. The result indicates negative values, that is, an enhanced acceleration of the zonal jet. The dashed line (1, −1, 2) describes the interaction with $n = 2$ where the topographic forcing exists. The result shows an increased energy supply at the end of the blocking episode. The dotted line describes the energy supply from synoptic disturbances of $n = 3$–6. There is an increased energy supply at the beginning and mature stages of the blocking episode. The solid line describes the sum of these three lines (see also Fig. 7). The results show that the important energy supply into $n = 1$ through the wave–wave interactions comes from synoptic disturbances. Robinson (1985) discussed a growth of $n = 1$ as an expense of energy of $n = 2$ as well as $n = 0$. Although the result in Fig. 7 exhibits wave 1–wave 2 vacillation, we find from Fig. 8 that the energy supply from topographic forcing appears to be of secondary importance for the blocking in the model.

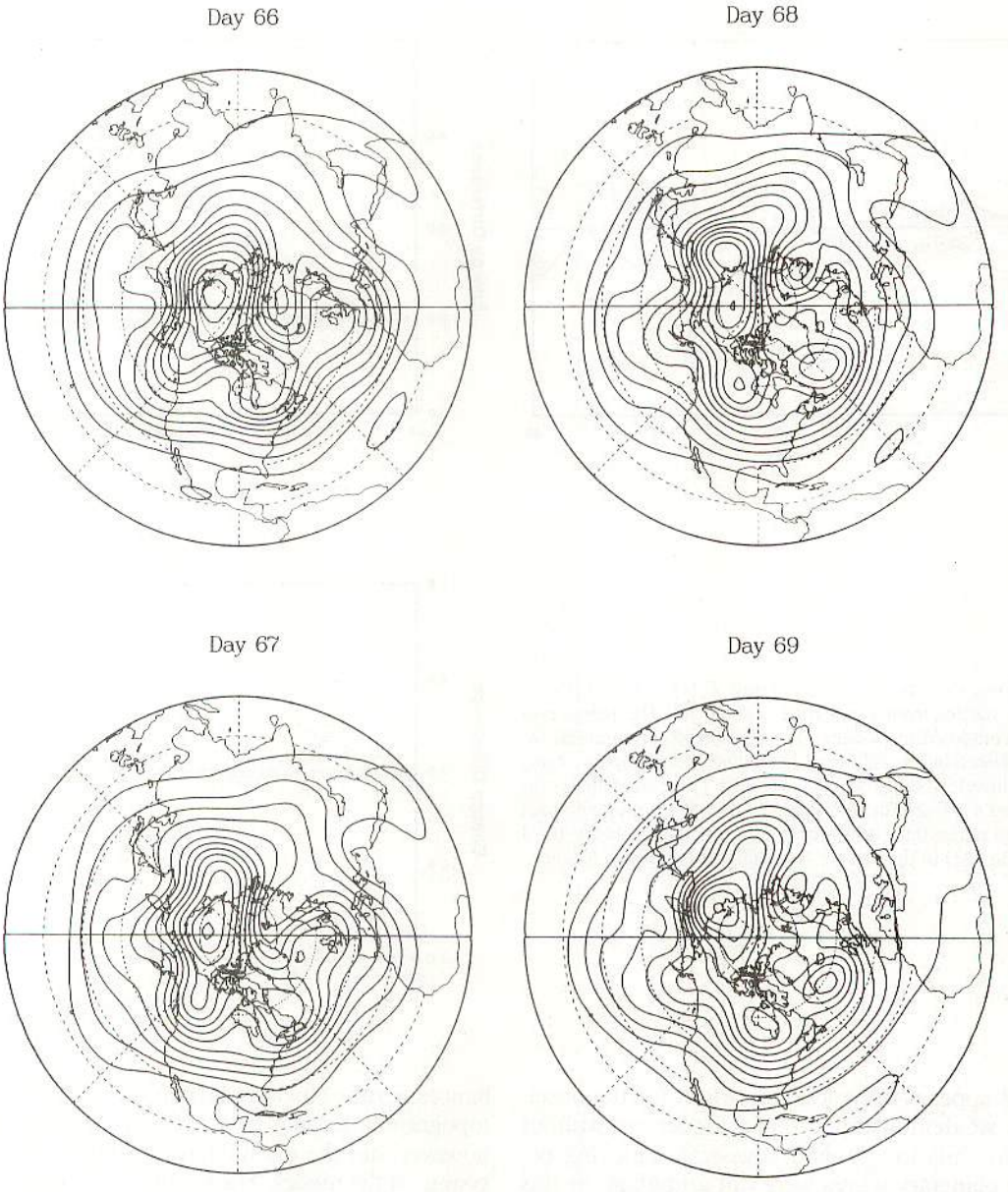

FIG. 6. (*Continued*)

4. Concluding summary

We have attempted in this study to simulate the amplifications of low-frequency planetary waves and concurrent blocking formations as realistically as possible, using a fully nonlinear numerical model that is as simple as possible. We have shown that a simple barotropic model with four physical processes (biharmonic diffusion, topographic forcing, baroclinic instability, and zonal surface stress) is sufficient to simulate a realistic and persistent dipole blocking, although these processes may not be the necessary conditions. The basic structure of the large-scale blocking is explained by a superposition of a meridional dipole structure of wavenumber 1 and a monopole structure of wavenumber 2. The problem in large-scale blocking is then focused on why these planetary waves are amplified.

There are two major energy sources in the model atmosphere: topographic forcing at wavenumber 2 and baroclinic instability in synoptic waves. These energy supplies in the system are transferred to other waves by the nonlinear wave–wave interactions. In this model the important amplification of low-frequency wavenumber 1 is caused by the nonlinear wave–wave interactions. A further analysis shows that the dipole-mode energy is transformed from synoptic disturbances originated by the parameterized baroclinic instability. The energy supply from topographic forcing at wave-

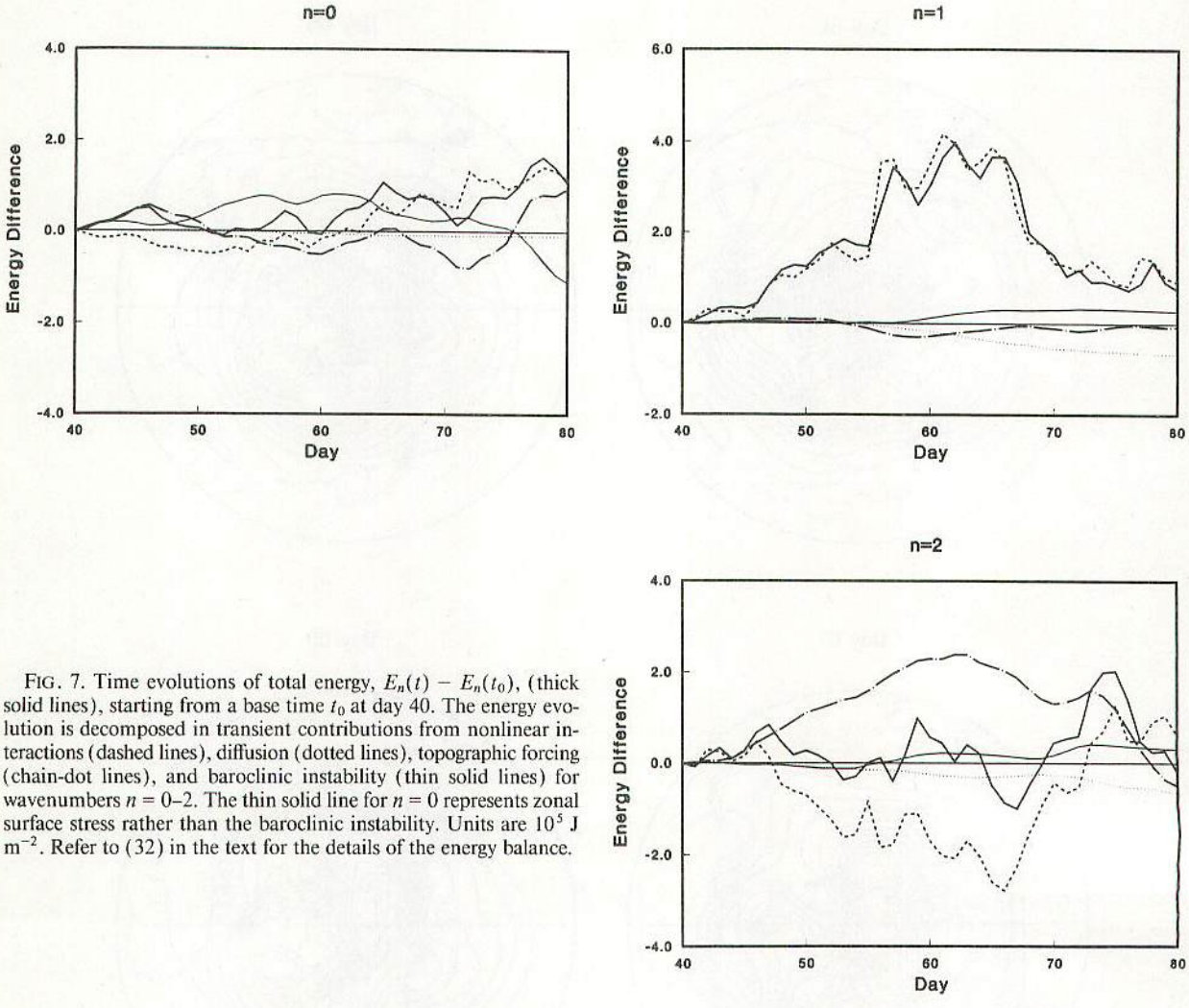

FIG. 7. Time evolutions of total energy, $E_n(t) - E_n(t_0)$, (thick solid lines), starting from a base time t_0 at day 40. The energy evolution is decomposed in transient contributions from nonlinear interactions (dashed lines), diffusion (dotted lines), topographic forcing (chain-dot lines), and baroclinic instability (thin solid lines) for wavenumbers $n = 0$–2. The thin solid line for $n = 0$ represents zonal surface stress rather than the baroclinic instability. Units are 10^5 J m^{-2}. Refer to (32) in the text for the details of the energy balance.

number 2 appears to be less important for the onset. However, we demonstrated that a model run without topography fails to simulate large-scale blocking because the planetary waves were not amplified. In this case, the synoptic-wave energy is transformed directly to the zonal flow. This implies that the triad interactions without topography are highly random except for the zonal-wave interactions, since the waves are excited by a linear process that operates individual waves. The result confirms that the large-scale, persistent zonal asymmetry is essential for a blocking formation (e.g., Kikuchi 1969; Malanotte-Rizzoli and Malguzzi 1987). Synoptic disturbances contribute to the amplification of wavenumber 1 and to the sharp transition from zonal to meridional flows only when the quasi-stationary planetary waves already exist. In this study, we showed that the persistent wavenumber 2 plays a catalytic role in drawing synoptic wave energy and feeding wavenumber 1.

This study demonstrated that excitations of both quasi-stationary planetary waves and synoptic disturbances permit blocking formations in the model. The topographic forcing in amplifying wavenumber 2 is, however, not the main energy source for the blocking system in the model. The results of our numerical simulation are summarized as follows:

(i) wavenumber 2 is amplified by the prescribed topographic forcing;

(ii) synoptic disturbances are excited by parameterized baroclinic instability;

(iii) under the quasi-stationary wavenumber 2, a meridional dipole mode of wavenumber 1 is amplified by the upscale energy cascade from synoptic disturbances;

(iv) basic futures of the blocking are created by the superposition of amplified wavenumbers 1 and 2, and the synoptic disturbances contribute to the sharp diffluent structure of the zonal jet.

It is discussed that the excitation mechanism of blocking is not unique. Instability of zonally varying basic state, transient forcing of a low-frequency com-

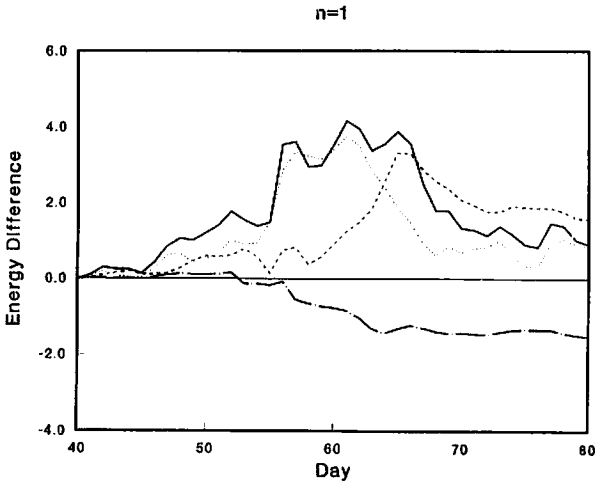

FIG. 8. Time evolutions of nonlinear interactions for $n = 1$ in Fig. 7, divided in contributions from downscale self-interactions with $n = 0$, that is, (1, 0, 1) for chain-dot line; upscale self-interactions with $n = 2$, that is, (1, −1, 2) for dashed line; and the rest of upscale triad interactions of (1, −2, 3), (1, −3, 4), (1, −4, 5), and (1, −5, 6) for dotted line. The solid line describes the sum of these three lines. Units are 10^5 J m^{-2}.

ponent, and direct topographic forcing are possible mechanisms. Among those, the vorticity forcing mechanism for dipole blocking by transient disturbances is supported by many recent studies (Shutts 1983; Hains and Marshall 1987; Vautard and Legras 1988; Hansen and Chen 1982; Holopainen and Fortelius 1987). The present study demonstrates the same mechanisms based on a primitive equation model on a sphere with an emphasis that steady planetary waves play a catalytic role in this process. Observational analyses, however, indicate considerable baroclinic conversions related to blocking formations and low-frequency variability (Shilling 1986; Sheng and Hayashi 1990; Dole and Black 1990). A recent study by Dole and Black (1990) suggests the importance of large-scale instability for three-dimensional climatological states (see Frederiksen 1982; Malanotte-Rizzoli and Malguzzi 1987). Further studies are necessary to show the relative importance of the transient forcing mechanism, the three-dimensional instability theory, and the direct topographic forcing for better understanding of the low-frequency variability.

Acknowledgments. This research was supported by the National Science Foundation under Grant ATM-8923064. The original manuscript was edited by C. Helfferich and D. Fitzgerald.

APPENDIX

A Life Cycle of Nonlinear Baroclinic Waves

Simmons and Hoskins (1978) conducted a numerical simulation of a life cycle of nonlinear baroclinic waves. According to their simulations, an initial perturbation superimposed on a zonal field grows exponentially by baroclinic instability drawing zonal available potential energy. The amplified baroclinic waves start to transfer the energy back to the zonal kinetic energy by the barotropic conversion. The nonlinear baroclinic waves appear to accelerate the zonal jet at the end of their life cycle.

In the present study, the life-cycle experiment is demonstrated for the Simmons and Hoskins 45° jet with initial perturbations of $n = 6$ by integrating the three-dimensional spectral model of (11). A sole physics of the biharmonic diffusion similar to (17) is used in the simulation. Figure A1 illustrates the results of energy evolution and corresponding energy transfor-

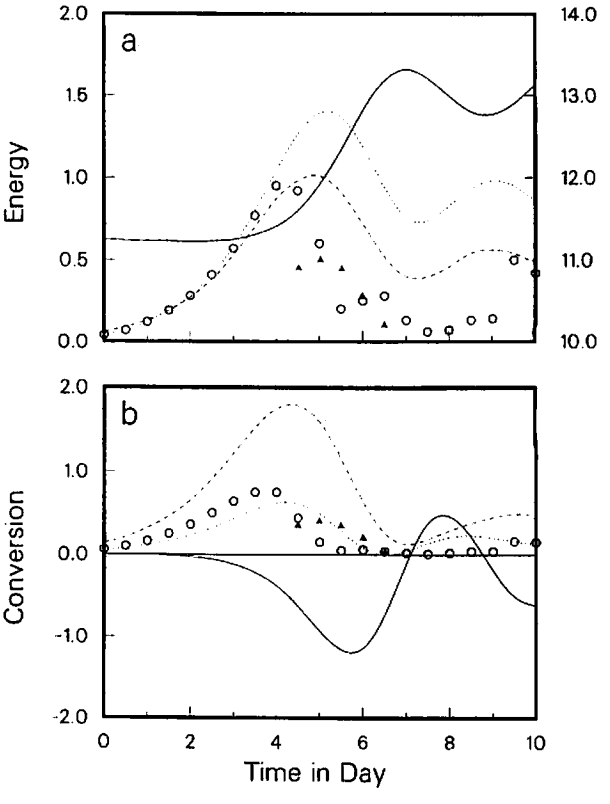

FIG. A1. (a) Time variation of eddy baroclinic energy (dashed line), eddy barotropic energy (dotted line), and zonal barotropic energy (solid line with the right ordinate) for wavenumber 6 disturbances. Units are in 10^5 J m^{-2}. The eddy barotropic energy is projected onto the most unstable mode (circles) according to (24). The fastest-growing Charney mode is stabilized and is replaced by other most unstable mode (triangles) for days 4.5–6.5. The circles are the second unstable modes during this period. (b) Time variation of various energy transformations associated with the energy variations. The dashed line is for a transformation from zonal baroclinic to eddy baroclinic energies, the dotted line is from eddy baroclinic to eddy barotropic energies, and the solid line is from zonal barotropic to eddy barotropic energies. Units are in watts per square meter (W m^{-2}). Parameterized energy transformations from eddy baroclinic to eddy barotropic energies according to (26) are plotted with circles and triangles. The triangles for days 4.5–6.5 are the most unstable modes, and the circles are the second unstable modes during this period.

mations in the framework of baroclinic–barotropic decomposition of atmospheric energy (see Tanaka and Kung 1989). The energy transformations from the zonal baroclinic to eddy barotropic components in their Fig. 8 are rearranged in this study so that the transformations pass through the eddy baroclinic components. Similarly, the transformations from the zonal barotropic to eddy baroclinic components are rearranged so that they pass through the eddy barotropic components.

The initial perturbations of $n = 6$ grow exponentially drawing zonal baroclinic energy. This early evolution is reasonably described by linear baroclinic instability of the 45° jet. Both the baroclinic energy (dashed line) and barotropic energy (dotted line) of $n = 6$ increase simultaneously since the unstable mode maintains its consistent structure to grow. The energy flow is characterized as from zonal baroclinic energy via eddy baroclinic energy and eddy barotropic energy. These energy transformations are also synchronized, since they are proportional to the eddy energy levels in the linear framework. When the waves reach finite amplitude, the barotropic conversion (solid line) increases, transferring the eddy barotropic energy toward zonal barotropic energy. As a result, zonal barotropic energy increases when the waves decay. It is shown that the zonal jet is accelerated so that the structure becomes more barotropic. The results are consistent with previous studies (e.g., Hoskins 1983).

The important process in baroclinic instability is the eddy heat flux due to the downscale zonal-wave interaction and baroclinic conversion. The early stage of this baroclinic conversion is fundamentally a linear process. In contrast, the upscale zonal-wave interaction of the barotropic conversion is essentially a nonlinear process. We find that the important baroclinic–barotropic interactions (dotted line of Fig. A1b) are coupled with baroclinic instability rather than the barotropic conversion. The applicability of the parameterization at the finite amplitude is examined here.

The orthogonal projection in (24) (circles in Fig. A1a) accounts for the major part of the eddy barotropic energy during the early stage, indicating the dominant linear process. Since the baroclinic–barotropic interaction attains its maximum at day 4 and decreases later (dotted line in Fig. A1b), the parameterization should deviate from the exponential energy growth to reduce the energy conversion. At day 4, the orthogonal projection decreases substantially, while the barotropic energy keeps increasing. The resulting reduction in the energy conversion is consistent with the nonlinear model results. As the zonal field varies by the activities of the unstable waves, the fast-growing Charney mode (circles) is stabilized and is replaced by the other unstable mode (triangles). In Fig. A1b, the energy supply due to the parameterized baroclinic instability (circles and triangles) agrees reasonably well with the model result even at the mature stage. Hence, the parameterization of baroclinic instability in sections 2–4 may be justified as the first approximation of the baroclinic–barotropic interactions. The parameterization tends to overestimate the energy supply at the finite amplitudes and is poor when the most unstable mode changes. However, in the observed atmosphere under the continuous differential heating, the Charney mode is the dominant mode most of the time.

REFERENCES

Andrews, D. G., J. H. Holton and C. B. Leovy, 1987: Middle Atmosphere Dynamics. Academic Press, 489 pp.

Charney, J. G., and A. Eliassen, 1949: A numerical method for predicting the perturbations of the middle-latitude westerlies. *Tellus*, **1**, 38–54.

——, and J. G. DeVore, 1979: Multiple flow equilibria in the atmosphere and blocking. *J. Atmos. Sci.*, **36**, 1205–1216.

Chen, T.-C., and J. Shukla, 1983: Diagnostic analysis and spectral energetics of a blocking event in the GLAS climate model simulation. *Mon. Wea. Rev.*, **111**, 3–22.

——, and K. E. Trenberth, 1988: Forced planetary waves in the Northern Hemisphere winter: Wave coupled orographic and thermal forcings. *J. Atmos. Sci.*, **45**, 657–680.

Dole, R. M., 1986: The life cycle of persistent anomalies and blocking over the North Pacific. *Adv. Geophys.*, **29**, 31–69.

——, and R. X. Black, 1990: Life cycles of persistent anomalies. Part II: The development of persistent negative height anomalies over the North Pacific Ocean. *Mon. Wea. Rev.*, **118**, 824–846.

Frederiksen, J. S., 1982: A unified three-dimensional instability theory of the onset of blocking and cyclogenesis. *J. Atmos. Sci.*, **39**, 969–982.

——, and R. C. Bell, 1987: Teleconnection patterns and the role of baroclinic, barotropic, and topographic instability. *J. Atmos. Sci.*, **44**, 2200–2218.

Haines, K., and J. Marshall, 1987: Eddy-forced coherent structures as a prototype of atmospheric blocking. *Quart. J. Roy. Meteor. Soc.*, **113**, 681–704.

Hansen, A. R., and T.-C. Chen, 1982: A spectral energetics analysis of atmospheric blocking. *Mon. Wea. Rev.*, **110**, 1146–1165.

Holloway, J. L., Jr., M. J. Spelman and S. Manabe, 1973: Latitude–longitude grid suitable for numerical time integration of a global atmospheric model. *Mon. Wea. Rev.*, **101**, 69–78.

Holopainen, E., and C. Fortelius, 1987: High-frequency transient eddies and blocking. *J. Atmos. Sci.*, **44**, 1632–1645.

Hoskins, B. J., 1983: Modelling of the transient eddies and their feedback on the mean flow. Large-scale Dynamical Processes in the Atmosphere. B. J. Hoskins and R. P. Pearce, Eds., Academic Press, 169–199.

Jacqmin, D., and R. S. Lindzen, 1985: The causation and sensitivity of the Northern Hemisphere planetary waves. *J. Atmos. Sci.*, **42**, 724–745.

Juckes, M., 1989: A shallow water model for the winter stratosphere. *J. Atmos. Sci.*, **46**, 2934–2955.

Kasahara, A., 1977: Numerical integration of the global barotropic primitive equations with Hough harmonic expansions. *J. Atmos. Sci.*, **34**, 687–701.

Kikuchi, Y., 1969: Numerical simulation of the blocking process. *J. Meteor. Soc. Japan.*, **47**, 29–54.

Kung, E. C., H. L. Tanaka and W. E. Baker, 1989: Energetics examination of winter blocking simulations in the Northern Hemisphere. *Mon. Wea. Rev.*, **19**, 2019–2040.

Malanotte-Rizzoli, P., and R. Malguzzi, 1987: Coherent structures in a baroclinic atmosphere. Part III: Blocking formation and eddy forcing. *J. Atmos. Sci.*, **44**, 2493–2505.

Nakamura, H., M. Tanaka and J. M. Wallace, 1987: Horizontal structure and energetics of Northern Hemisphere wintertime teleconnection patterns. *J. Atmos. Sci.*, **44**, 3377–3391.

Namias, J., 1950: The index cycle and its role in the general circulation. *J. Meteor.*, **7**, 130–139.

Phillips, N. A., 1959: Numerical integration of the primitive equations on the hemisphere. *Mon. Wea. Rev.*, **87**, 333–345.

Plumb, R. A., 1981: Instability of the distorted polar night vortex: A theory of stratospheric warming. *J. Atmos. Sci.*, **38**, 2514–2531.

Robertson, A. W., and W. Mets, 1989: Three-dimensional linear instability of persistent anomalous large-scale flows. *J. Atmos. Sci.*, **46**, 2783–2801.

Robinson, W. A., 1985: A model of the wave 1–wave 2 vacillation in the winter stratosphere. *J. Atmos. Sci.*, **42**, 2289–2304.

Salby, M. L., R. R. Garcia, D. O'Sullivan and J. Tribbia, 1990: Global transport calculations with an equivalent barotropic system. *J. Atmos. Sci.*, **47**, 188–214.

Saltzman, B., 1957: Equations governing the energetics of the larger scales of atmospheric turbulence in the domain of wave number. *J. Meteor.*, **14**, 513–523.

Sheng, J., and Y. Hayashi, 1990: Estimation of atmospheric energetics in the frequency domain during the FGGE year. *J. Atmos. Sci.*, **47**, 1255–1268.

Shilling, H.-D., 1986: On atmospheric blocking types and blocking numbers. Anomalous Atmospheric Flows and Blocking. *Adv. Geophys.*, **29**, 71–99.

Shutts, G. J., 1983: The propagation of eddies in diffluent jet streams: Eddy vorticity forcing of blocking flow fields. *Quart. J. Roy. Meteor. Soc.*, **109**, 737–761.

Silva Dias, P. L., and J. P. Bonatti, 1986: Vertical mode decomposition and model resolution. *Tellus*, **38A**, 205–214.

Smagorinsky, J., 1963: General circulation experiments with the primitive equations. I. The basic experiment. *Mon. Wea. Rev.*, **91**, 99–164.

Swarztrauber, P. N., and A. Kasahara, 1985: The vector harmonic analysis of Laplace's tidal equation. *SIAM J. Sci. Stat. Comput.*, **6**, 464–491.

Tanaka, H. L., 1985: Global energetics analysis by expansion into three-dimensional normal mode functions during the FGGE winter. *J. Meteor. Soc. Japan.*, **63**, 180–200.

——, and E. C. Kung, 1988: Normal mode energetics of the general circulation during the FGGE year. *J. Atmos. Sci.*, **45**, 3723–3736.

——, and ——, 1989: A study of low-frequency unstable planetary waves in realistic zonal and zonally varying basic states. *Tellus*, **41A**, 179–199.

——, and S. Sun, 1990: A study of baroclinic energy source for large-scale atmospheric normal modes. *J. Atmos. Sci.*, **47**, 2674–2695.

——, E. C. Kung and W. E. Baker, 1989: Normal mode energetics and error analysis of GLA GCM simulations with different horizontal resolutions during a winter month. *Beitr. Phys. Atmos.*, **62**, 99–111.

Tung, K. K., and R. S. Lindzen, 1979: A theory of stationary long waves. Part I: A simple theory of blocking. *Mon. Wea. Rev.*, **107**, 714–734.

Valdes, P. J., and B. J. Hoskins, 1989: Linear stationary wave simulations for the time-mean climatological flow. *J. Atmos. Sci.*, **46**, 2509–2527.

Vautard, R., and B. Legras, 1988: On the source of midlatitude low-frequency variability. Part II: Nonlinear equilibration of weather regimes. *J. Atmos. Sci.*, **45**, 2845–2867.

Wiin-Nielsen, A., 1962: On transformation of kinetic energy between the vertical shear flow and the vertical mean flow in the atmosphere. *Mon. Wea. Rev.*, **90**, 311–323.

——, 1986: Global scale circulations—a review. Anomalous Atmospheric Flows and Blocking. *Adv. Geophys.*, **29**, 3–27.